

Numerical Investigation of Separated Nozzle Flows

C. L. Chen* and S. R. Chakravarthy†

Rockwell International Science Center, Thousand Oaks, California 91360

and

C. M. Hung‡

NASA Ames Research Center, Moffett Field, California 94035

A numerical study of axisymmetric overexpanded nozzle flows is presented. The flow structures of the startup and throttle-down processes are examined. During the impulsive startup process, observed flow features include the Mach disk, separation shock, Mach stem, vortex core, contact surface, slip stream, initial shock front, and shocklet. Also the movement of the Mach disk is not monotonical in the downstream direction. For a range of pressure ratios, hysteresis phenomenon occurs; different solutions were obtained depending on different processes. Three types of flow structures were observed. The location of separation point and the lower end turning point of hysteresis are closely predicted. A high peak of pressure is associated with the nozzle flow reattachment. The reversed vortical structure trapped behind the Mach disk appears to be key to causing the differences in the flow structures and affects engine performance.

Nomenclature

| | |
|------------|---|
| a_∞ | = ambient sound speed |
| C_F | = thrust coefficient |
| C_{Fopt} | = thrust coefficient for an optimum expansion nozzle |
| CS | = initial contact surface |
| C_T | = thrust efficiency, C_F/C_{Fopt} |
| p_a | = ambient pressure |
| p_c | = chamber total pressure |
| PR | = pressure ratio, p_c/p_a |
| R_t | = radius of throat |
| SF | = initial shock front |
| SL | = shocklet |
| TP | = triple point |
| V | = vortex core |
| x, y | = Cartesian coordinates, origin is at center of nozzle throat |
| γ | = ratio of specific heats |

I. Introduction

A TYPICAL inviscid one-dimensional nozzle flow can be characterized into four types as shown in Fig. 1, depending on its corresponding ambient pressure. An overexpanded nozzle flow is shown as type III under pressure condition 5 in Fig. 1, where condition 4 indicates an internal shock standing right at the exit plane, and condition 6 is the design condition,¹ i.e., the exit pressure is equal to the ambient pressure. Ideally, the overexpanded nozzle flow is supersonic within the entire portion of the nozzle downstream of the throat, and the exit-plane pressure is uniformly lower than the ambient pressure. However, for an actual nozzle under ambient pressure condition 5, complicated shock wave and boundary-layer interactions can lead to the separation of the boundary layer on the nozzle wall and result in a highly nonuniform flow at the nozzle exit plane.² The flow separation not only affects nozzle performance but also can cause severe damage to the structure.³ The intri-

cacies of the side-load problem and the three-dimensional tepee-type separation present challenges and issues that are the motivation for this research work.

The main objective of the present effort is to understand separated overexpanded nozzle flows using a time-accurate compressible Navier-Stokes solver. A 1/16-scale nozzle of a J-2S rocket engine⁴ (area ratio: 39.6, nozzle length: 87.72 in., throat radius: 6.1 in.), which was a precedent of the Space Shuttle main engine (SSME), is used as the model for the present study. There are sufficient cold-flow data available, and the nozzle's separated flow structure is similar to that of the SSME. Specific aspects emphasized in the discussion are 1) investigation of transient nozzle flow evolution during a startup process, 2) analysis of the overall flow structures in an overexpanded nozzle, and 3) the hysteresis phenomenon.

Although the scope of the present study is restricted to the axisymmetric flowfield without swirling, the importance of the asymmetric flow structure to an axisymmetric nozzle should never be ignored. The investigation of the more realistic three-dimensional flow structure will be a continuation of the present work.

II. Numerical Approach

The equations solved here are the unsteady, axisymmetric Reynolds-averaged compressible Navier-Stokes equations with a turbulence model used for closure. The perfect gas relation and a constant ratio of specific heats are used in the computation. The time-

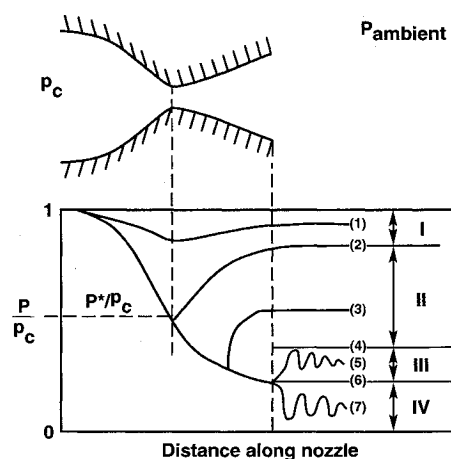


Fig. 1 Pressure vs distance for converging-diverging nozzle with various pressure ratios.

Received July 29, 1993; revision received April 19, 1994; accepted for publication April 22, 1994. Copyright © 1994 by the American Institute of Aeronautics and Astronautics, Inc. Under the copyright claimed herein, the U.S. Government has a royalty-free license to exercise all rights for Governmental purposes. Rockwell International reserves all proprietary rights other than copyright; the author(s) retain the right of use in future works of their own; and Rockwell International reserves the right to make copies for its own use, but not for sale. All other rights are reserved by the copyright owner.

*Member Technical Staff, Computational Fluid Dynamics Department. Member AIAA.

†Manager, Computational Fluid Dynamics Department. Member AIAA.

‡Research Scientist, Fluid Dynamics Division. Associate Fellow AIAA.

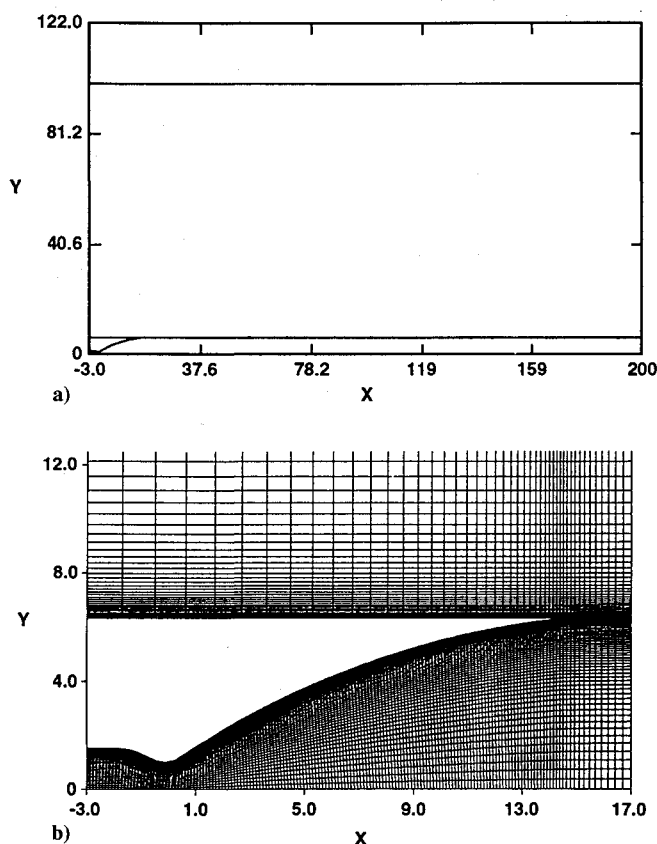


Fig. 2 Grid used in the nozzle flow: a) zonal topology and b) overall grid distribution.

accurate unified solution algorithm (USA) Navier-Stokes code is employed to calculate the separated nozzle flow. Time accuracy is required to study the transient flow and the unsteady nature of the separated flow due to shock/boundary-layer/shear-layer interaction. The USA code, which is a finite-volume multizonal Navier-Stokes solver, utilizes a high-resolution total variation diminishing (TVD) scheme. This code was validated from low subsonic to hypersonic flows. Details of the USA code can be found in Ref. 5. The turbulence model used here is a modified version of the Baldwin-Lomax model.⁶ Although other transport equation models were tried in this study, this model appeared to be the most robust and always provided consistent results without regard to chamber boundary condition and initial condition specification for the turbulence quantities.

A two-zone grid (inner and outer) was used in this study. The nozzle configuration and overall grid distribution are shown in Fig. 2. The nozzle throat is at $x = 0.0$, and the nozzle exit is at $x = 14.38$ (nondimensionalized by throat radius). The nozzle exit radius is $y = 6.29$. The inner zone is from the chamber to the downstream outflow boundary, which is located 200 radii downstream of the nozzle throat; the outer zone covers the nozzle wall to the far field, which is 100 radii away. The zonal boundary is located at the nozzle lip extension interface. The grid points are clustered around the nozzle configuration, especially near the nozzle wall.

The numerical boundary conditions used in this work are zonal boundary, far-field characteristic boundary condition, and adiabatic no-slip wall and symmetry boundary condition. The chamber boundary condition is implemented with fixed total pressure, upstream Riemann invariant, zero flow angle, and extrapolated downstream Riemann invariant. The ratio of the chamber total pressure p_c to ambient pressure p_a varies from 20, 30, 32, 35, and 45 to 65. For area ratio 39.6, the pressure ratio $PR = p_c/p_a$ is about 1030 at condition 6 and 28 at condition 4 in Fig. 1. Therefore, except for pressure ratio 20, all of the cases studied belong to over-expanded nozzle flows. The chamber temperature (300 K) was

chosen the same as the ambient condition, and the chamber density varied in proportion to pressure ratios. The centerline Mach number at the nozzle inlet was 0.265. The unit Reynolds number at inlet varied from 120 to 400 million.

The computations start with either an impulsive or sequential startup (or throttle-down) process. For the impulsive startup process, the initial condition is quiescent everywhere, except that the chamber condition is prescribed inside the constant duct portion, ahead of the converging part of the nozzle. The pressure-jump diaphragm is located at the beginning of the area convergent. For the sequential startup (or throttle-down) process, the initial flowfield is a previously computed flowfield along with the new prescribed chamber pressure at the inflow location.

Three sets of grids were used to determine if there are sufficient grid points. The first (coarse) grid set has 151×71 grid points for the inner zone and 84×71 for the outer zone. The minimum grid space normal to the wall is 0.001 radius ($y^+ \leq 10$). A total of 101×71 grid points are inside the nozzle. The second grid set has $223 \times 91 + 106 \times 91$ grid points, with 151×91 grid points inside the nozzle. The minimum grid space normal to the wall is 0.0001 radius ($y^+ \leq 2$). The results of this grid refinement study for the pressure ratio $PR = 45$ show no substantial differences with regard to the evolution of the Mach disk and the global flow structure inside the nozzle, except for a better capture of the thin boundary-layer profile. Furthermore, for the sake of caution, the third set grid was generated using the same minimum space as the second set and doubling the grid points in each direction. The existence of a centerline vortical structure behind the Mach disk outside of the nozzle exit for the extreme case of $PR = 65$ is confirmed. Therefore, the second grid set is ensured sufficient for the remaining cases with various chamber pressures since the main flow features concerned here are not more than one nozzle length downstream of the nozzle exit plane. All of the results discussed here used this second grid set.

The size of the time step was also examined for the case of $PR = 45$. The transient flow solutions remain accurate when the Courant-Friedrichs-Lewy (CFL) number is increased to 20 (the size of the time step is chosen as the minimum time step allowed for all of the grid points; it is proportional to the CFL and inversely proportional to the largest eigenvalue). Therefore, a CFL of 20 or less is used in all of the computations reported here.

III. Results and Discussion

A. Impulsive Startup Nozzle Flow

Several time sequences of schlieren-type snapshots (magnitude of density gradient) are presented in Fig. 3 to illustrate the starting process. The large gradient is colored black. The computation starts impulsively, and the pressure ratio is assigned to be 45. The time was nondimensionalized by throat radius divided by reference velocity ($a_\infty/\sqrt{\gamma}$). The flow is complicated and intriguing: the schlieren-type plots have allowed clear identification of the initial contact surface (CS), slip stream behind the triple point (TP), shear layer due to the boundary-layer separation, initial shock front (SF) and various sequential types of vortical and shock structure. The overall snapshots show how the flowfield evolves from a vortical structure into a supersonic jet directed downstream. This supersonic jet is confined by the separated boundary-layer flow and the slip stream. The contact surface disappears in the contour plot of the magnitude of the pressure gradient (Fig. 4) and, hence, can be further distinguished from shocks by comparing Figs. 3 and 4. On the other hand, features that appear as black bands in both figures are shocks and shocklets (SL). Several snapshots of the contours of vorticity are shown in Fig. 5. (The black color means a strong vorticity.) The association between shocklets and vortex cores (V) is further identified by comparing Figs. 4 and 5. Strong vorticity is generated by the separated boundary layer and the slip stream between the Mach disk and the Mach stem. The vortical structure induces shocklets, the shocklets induce the total pressure loss, and the curvature of the shock generates the entropy gradient and vorticity. The vortex and shocklets interact with each other. The shocklets sometimes disappear (for instance, Fig. 3c) and later re-

appear (Fig. 3f) standing around the vortex core. The core of the vortex has low total pressure, which can be attributed to the effects of shocks and viscous dissipation.

The Mach disk appears reluctant to leave the nozzle exit and does not move monotonically in the downstream direction. At the early stage of the startup process (Figs. 3a–3k), the Mach disk moves downstream and reaches about the nozzle exit (Fig. 3k). Then the Mach disk moves upstream and eventually settles at about $x/R_j = 10.8$ for the final state solution (Fig. 3p). In addition to the large-scale motion, the Mach disk moves with some small-scale oscillation during the startup process. The transient Mach disk strength can be much stronger than the final state solution. For instance, the pressure ratio across the Mach disk is 69.59 for Fig. 3k, higher than the final state 43.08 for Fig. 3p.

The supersonic jet is flapping during the developing stage, but eventually the unsteadiness amplitude is reduced. The final flow structure is fully separated with a triple point connecting separated shock, Mach disk, and Mach stem (or rear leg). We consider that

the flow has reached the final state when the basic flow structure is not changing except for a small oscillatory behavior that remains.

B. Process Dependent Nozzle Flow

1. Case of Chamber Pressure 65

The solution of pressure ratio 45 at nondimensional time about 80 is used as the initial condition for $PR = 65$. In Fig. 6, the instantaneous streamlines of a final state solution are overlaid on background pressure and Mach number shades. The low pressure is colored white in Fig. 6a. The Mach number close to one is colored black in Fig. 6b (subsonic is colored white). The supersonic jet is close to the nozzle wall and separated from the wall near the nozzle lip. The upper portion of the Mach disk is bent downstream, becoming an oblique shock, and intersects the separation shock as shown in Fig. 7. The instantaneous streamlines depict the existence of a region of reversed flow with trapped vortical structure behind the Mach disk. The centerline pressure dip shown in Fig. 8 is evidence of the vortex's existence. The oscillatory behavior of

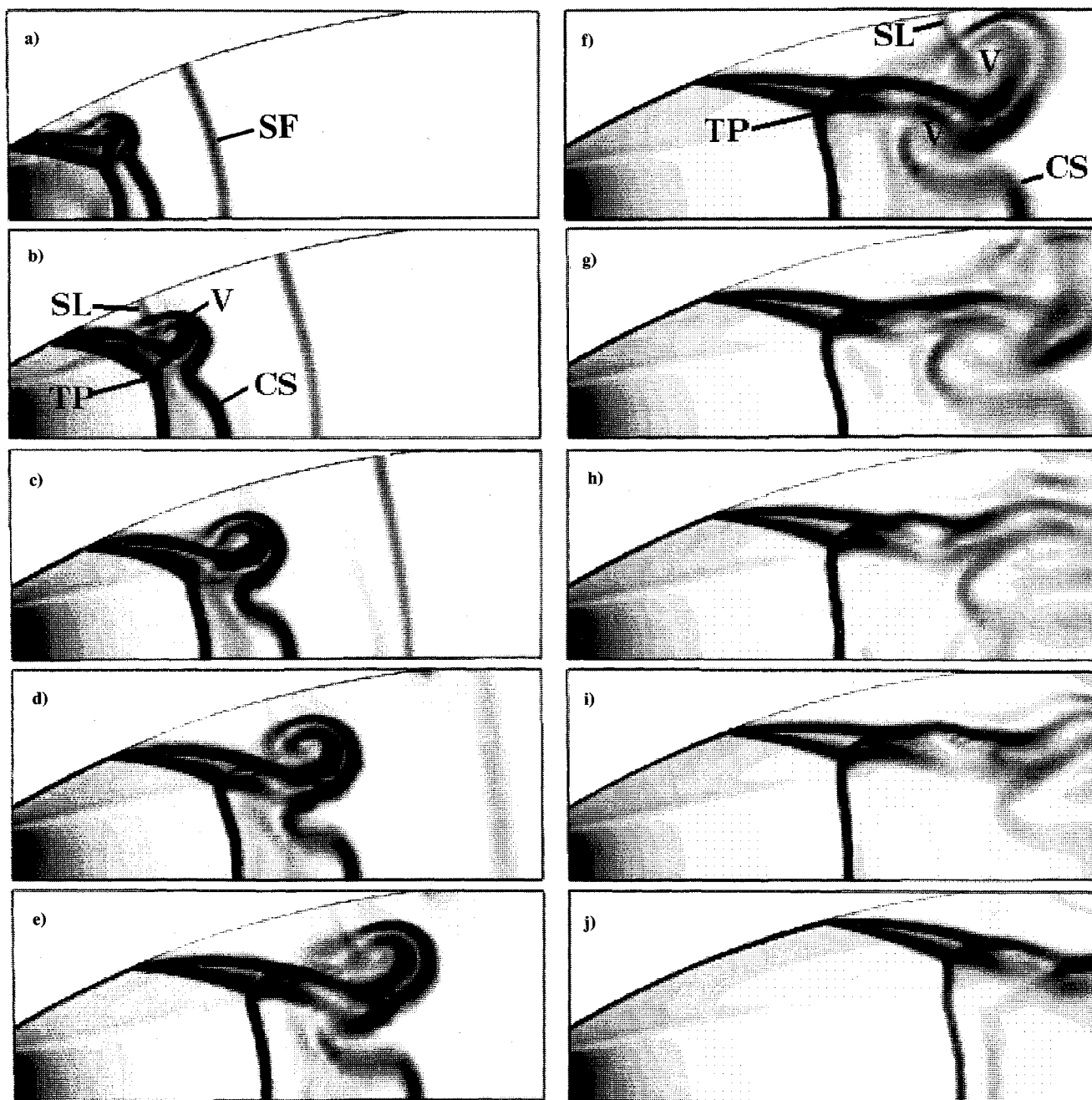


Fig. 3 Schlieren-type snapshots (magnitude of density gradient) in startup process, (x, y) at left low corner is $(1.8, 0)$: a) $t = 4.72$, b) $t = 6.43$, c) $t = 8.20$, d) $t = 10.06$, e) $t = 12.06$, f) $t = 14.04$, g) $t = 15.96$, h) $t = 17.90$, i) $t = 19.84$, j) $t = 29.26$.

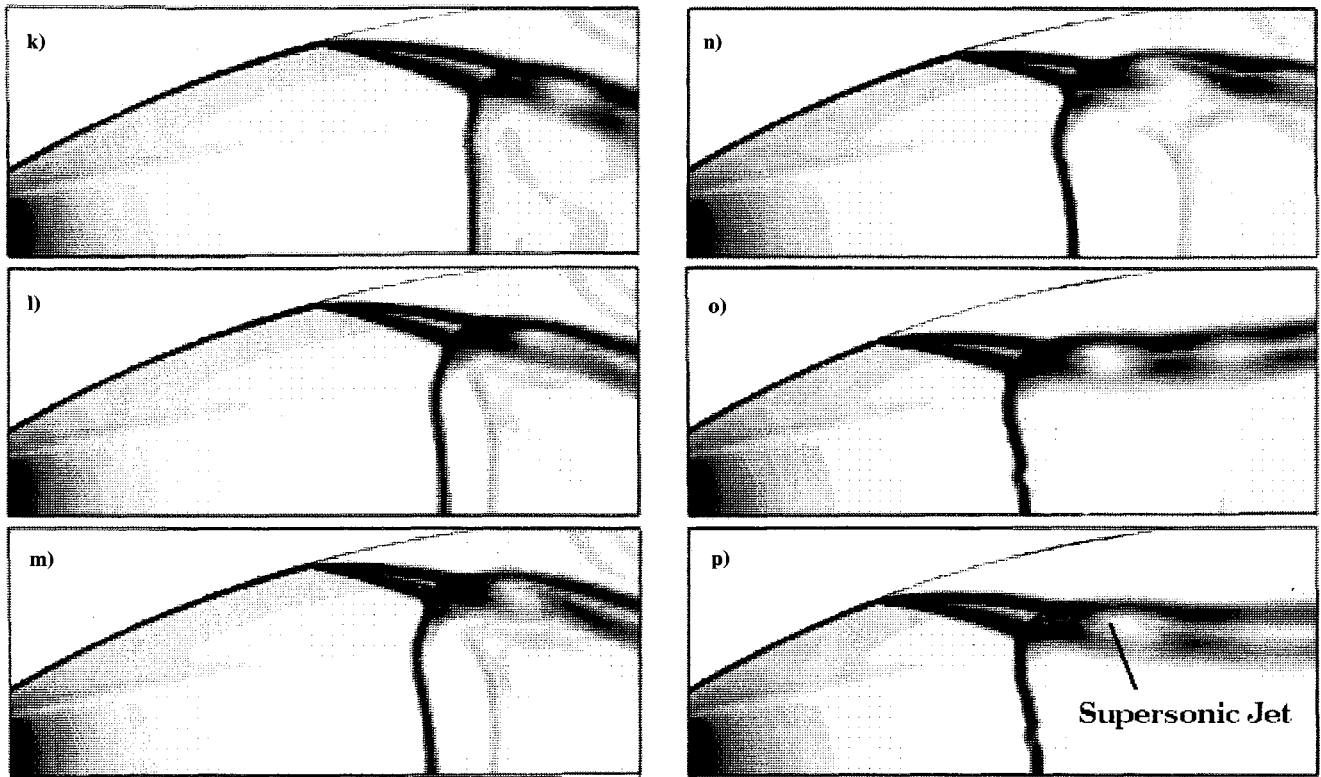


Fig. 3 (Continued) Schlieren-type snapshots (magnitude of density gradient) in startup process, (x, y) at left low corner is $(1.8, 0)$: k) $t = 31.16$, l) $t = 34.89$, m) $t = 36.77$, n) $t = 40.53$, o) $t = 98.21$, and p) $t = 246.6$.

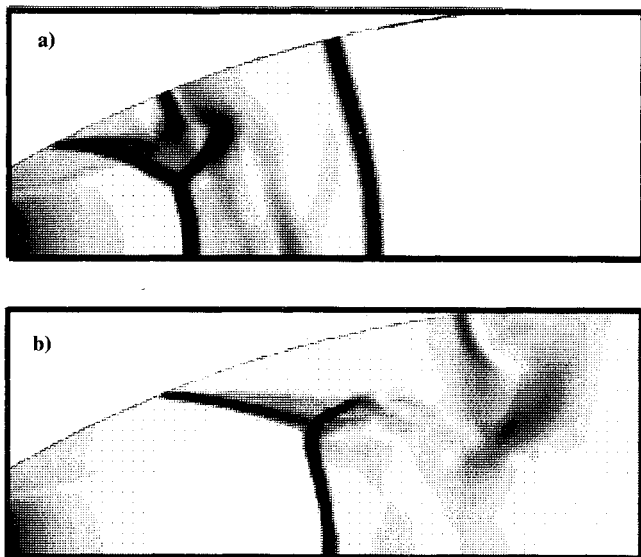


Fig. 4 Magnitude of pressure gradient corresponding to Figs. 3b and 3f; black means large pressure gradient.

the pressure distribution along the zonal boundary is caused by the expansion waves and compression waves interacting with the supersonic jet boundaries to match the ambient pressure. The computed trapped vortical structure was at least supported with 35 (streamwise) \times 20 (radial) grid points in this worst case. As mentioned earlier, we doubled the grid points in each direction (but retained the same minimum distance normal to the wall). This vortical structure remains there. A similar region of reversed flow behind the Mach disk in the transient stage for the case of $PR = 45$ (not shown here) was also observed. Nevertheless, that reversed flow eventually is convected downstream during the startup process.

The overall flow structure near the nozzle exit is described in Fig. 9. The spiral vortex was drawn to imply that unsteadiness may exist. The Mach disk is located near the exit plane of the nozzle. The flow remains fully separated from the wall but the separation point is very close to the nozzle lip. To the authors' knowledge, the phenomenon of a reversed flow with a vortex trapped behind the Mach disk for the nozzle flow has never been addressed. However, a loosely related flow model for the swirling nozzle flow can be found in Ref. 7.

2. Case of Pressure Ratio 45 (Throttle-Down Process)

The impulsive startup solution for pressure ratio 45 was discussed in Sec. III.A. Now the throttle-down process will be examined. The initial flowfield is from the solution of pressure ratio 65, and chamber pressure is suddenly reduced to 45. In Fig. 10, the instantaneous streamlines of a final state solution are again overlaid on background pressure and Mach number shades as case 1 in Sec. III.B. In this throttle-down process, the reversed vortical flow remain trapped behind the Mach disk and does not convect downstream. Such a vortical structure is further indicated by total pressure contours as shown in Fig. 11. The low total pressure is shown with the dark color, and the vortex core is represented by the low total pressure. For the vortex behind the Mach disk, total pressure contours follow the streamline patterns closely, but the pressure contours do not. This indicates that each streamline may have its own total pressure.

The supersonic jet remains near the nozzle wall and passes over the vortex core as case 1 in Sec. III.B. However, the separated flow induced by the separation shock is reattached to the wall as shown in Figs. 10 and 11. Topologically, a closed-type separation bubble is necessary for a steady two-dimensional separated flow. Even though the present solution is unsteady, its large structure is quite steady. The instantaneous streamlines behind the Mach disk and in the separated flow region next to the wall form almost closed loops.

The final state schlieren-type snapshots overlaid with instantaneous streamlines are compared with the startup solution in Fig. 12. Apparently, two solutions exist at the same pressure ratio and

are quite different from each other. Following the startup process, the separation shock occurs earlier (Fig. 12a). The flow is fully separated from the nozzle wall after the separation shock, and a clockwise separation bubble occurs near the nozzle lip. There is no reversed flow behind the Mach disk. After the throttling process, the flow is reattached to the nozzle wall, and there is a reversed flow behind the Mach disk (Fig. 12b). The existence of a large reversed flow region with a trapped vortical structure behind the

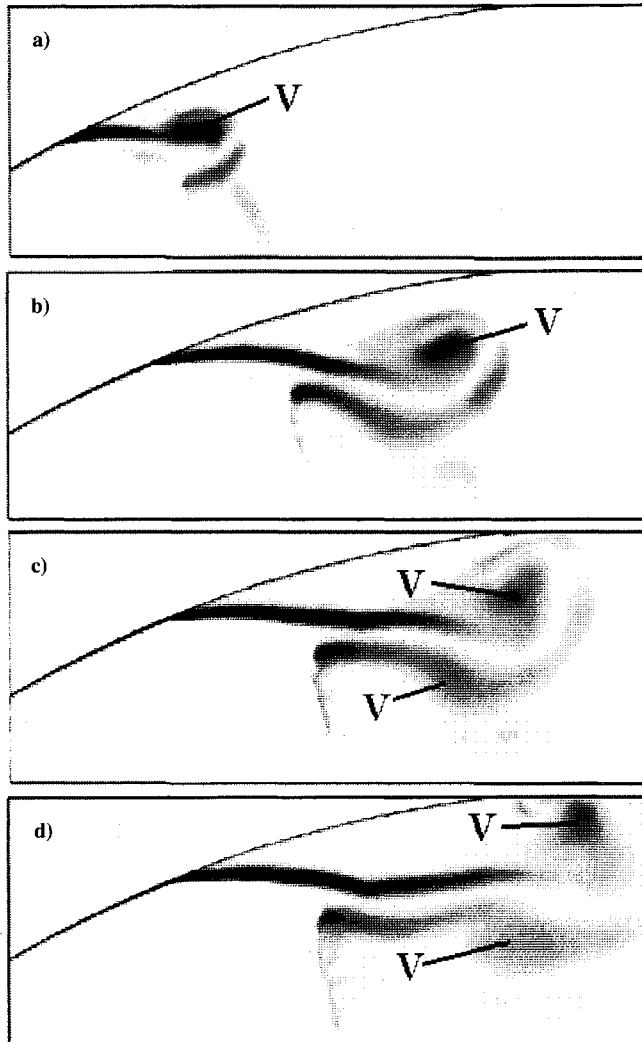


Fig. 5 Vorticity magnitude: a) corresponds to Fig. 3b, b) corresponds to Fig. 3e, c) corresponds to Fig. 3f, and d) corresponds to Fig. 3g; black means large vorticity.

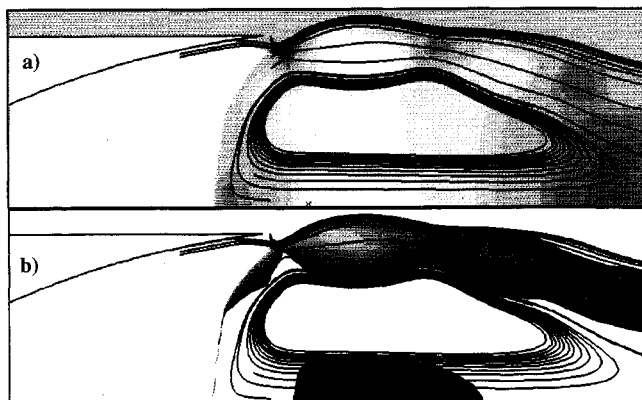


Fig. 6 Near nozzle lip results of startup process at $PR = 65$: a) instantaneous streamlines and pressure field and b) instantaneous streamlines and Mach number field.

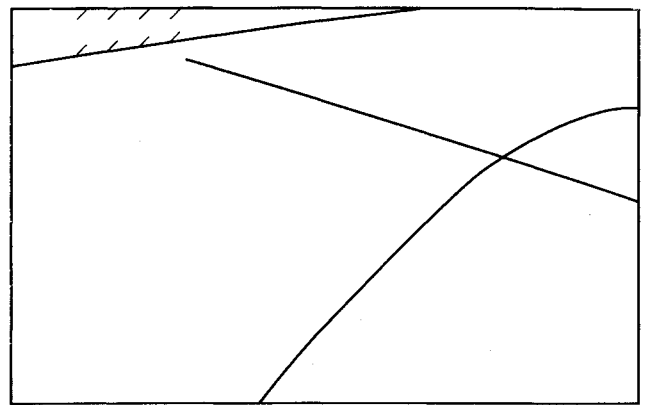


Fig. 7 Shock structure near the nozzle lip.

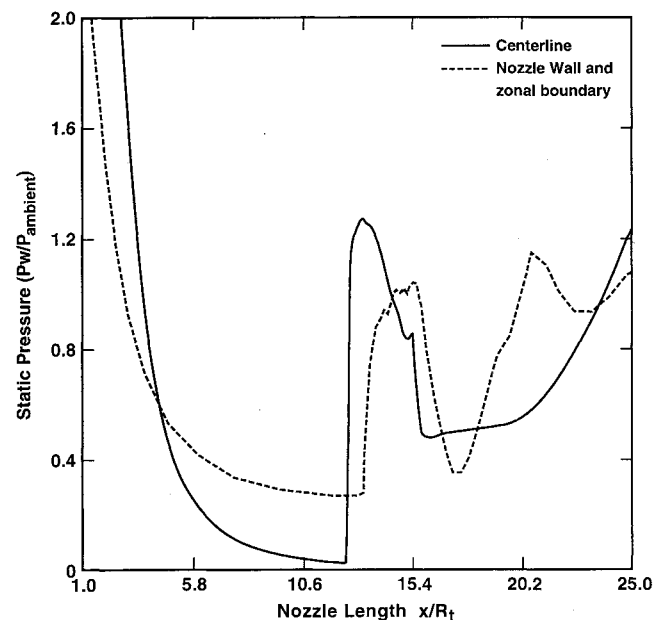


Fig. 8 Pressure distribution on the axis and nozzle wall.

Mach disk reduces performance following the throttle-down process. The thrust efficiency is reduced more than 12% (relative to the startup process).

The experimental schlieren photograph corresponding to the throttle-down process at pressure ratio 43 from Ref. 8 is also included, in Fig. 13. The fluid is flowing from right to left. Even though the experimental photograph illustrates only the nozzle exit flowfield, it does indicate the supersonic jet close to the nozzle wall for the throttle-down process. However, both the computational and experimental schlieren photograph could not show the existence of the trapped vortex because the magnitude of its density gradients is weaker than those associated with the shocks and slip streams.

The shock and flow structures are further outlined in Fig. 14. For the startup process (Fig. 14a), the triple point and Mach stem are far away from the nozzle wall, there is no reversed flow behind the Mach disk away from the wall, and the outer fluids are entrained into the nozzle (separated from the nozzle lip and attached to inner nozzle wall to form a clockwise separation bubble); whereas for the throttle-down process (Fig. 14b), the point of shock intersection and the Mach stem are close to the wall, there is a reversed flow behind the Mach disk away from the wall, and the inner nozzle flow separated from the wall but reattached to the wall to form a counterclockwise separation bubble. In Fig. 9, a clockwise separated bubble close to the lip, the same as in Fig. 14a, existed but was not shown because it was very small. The

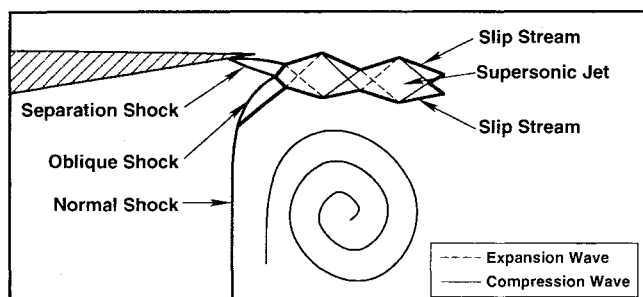


Fig. 9 Overall near nozzle lip flow structure for the case of $PR = 65$.

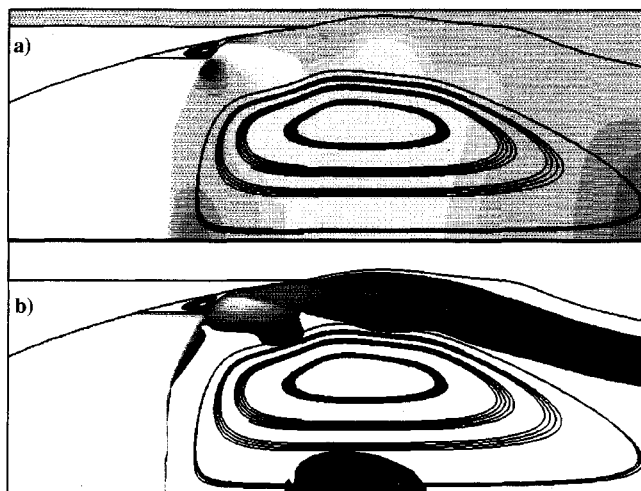


Fig. 10 Results near nozzle lip of throttle-down process at $PR = 45$: a) instantaneous streamlines and pressure field and b) instantaneous streamlines and Mach number field.

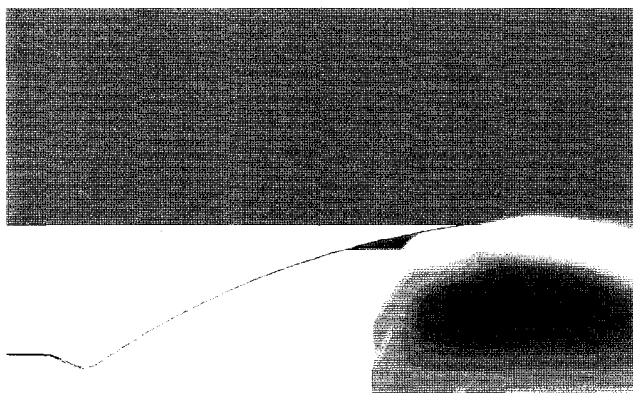


Fig. 11 Total pressure contours for the case of $PR = 45$.

main difference between Fig. 14b and Fig. 9 is this separated flow structure close to the wall. The high-pressure peak associated with this attachment in Fig. 14b will be shown later. On the other hand, the difference between Fig. 14a and Fig. 9 is the existence of reversed flow structure trapped behind the Mach disk. The type I, type II, and type III flows are used to distinguish the flow structures among Fig. 14a, Fig. 9, and Fig. 14b and will be discussed further.

C. Low-End Turning-Point of Hysteresis

The preceding discussions show that multiple solutions occur at the same pressure ratio. The question of whether or when the throt-

tled flow would come back to the same flow topology as the startup process (Fig. 3p) was examined next. Therefore, the chamber pressure was continuously reduced to investigate what would happen to the flowfield.

The solution obtained during the previous throttle-down case ($PR = 45$) is chosen as the initial condition for the sequential throttling process. The pressure ratio is reduced to 35, 32, and 30. The schlieren-type snapshot for $PR = 35$ with overlaid instantaneous streamlines is shown in Fig. 15. The flow remains reattached (type III), but the separation region near the wall becomes larger than the case of $PR = 45$. The Mach disk moves upstream and shock bending is reduced, but more shocklets appear. Similar flow structure occurs at $PR = 32$ (not shown here). When the chamber pressure finally drops to 30, the trapped vortex can no longer stand behind the Mach disk and is convected downstream. The flow topology goes back to a fully separated flow structure (type I) as shown in Fig. 16, which is the same as Fig. 12a.

The computed thrust efficiency varying with chamber pressure is compared with the experimental measurements in Fig. 17. The three type flows are also identified in this figure. The thrust efficiency C_T is defined as the thrust obtainable from an actual nozzle at some specified pressure ratio operating condition divided by the

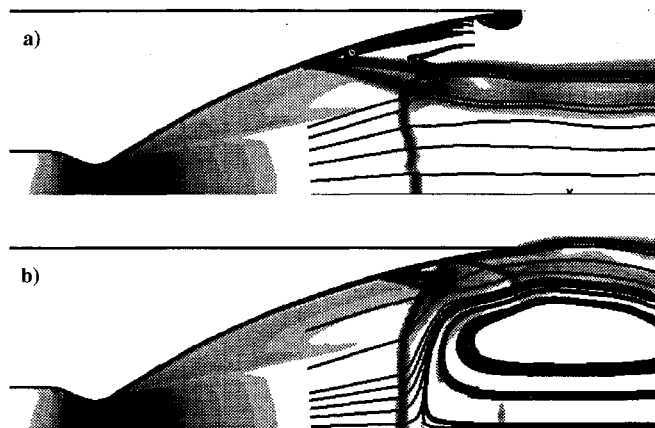


Fig. 12 Schlieren-type snapshots, $PR = 45$: a) startup process and b) throttle-down process.

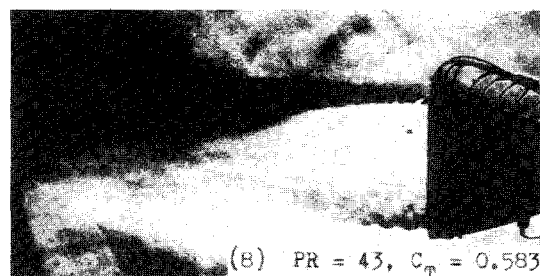
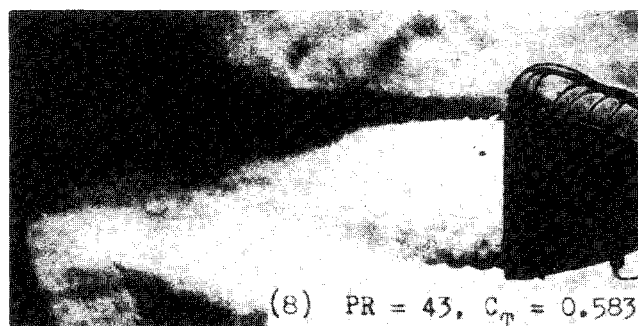


Fig. 13 J-2S model schlieren photograph.

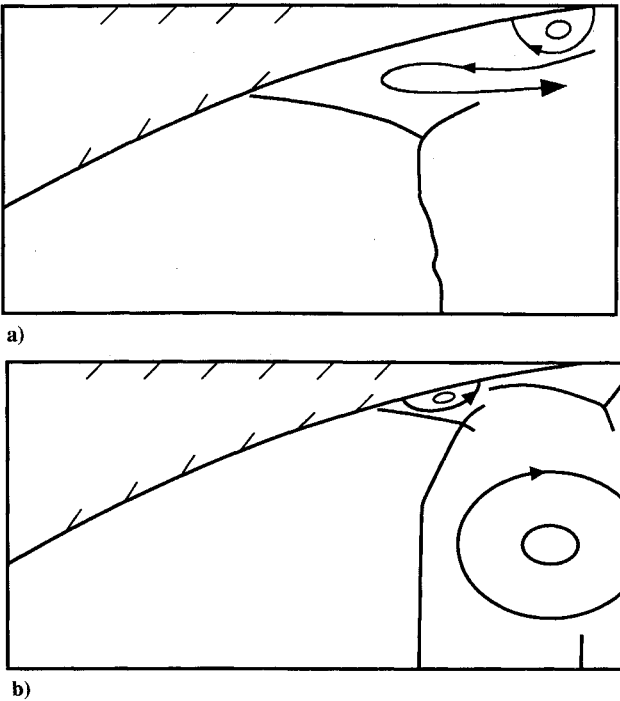


Fig. 14 Shock structures for $PR = 45$: a) startup process and b) throttle-down process.

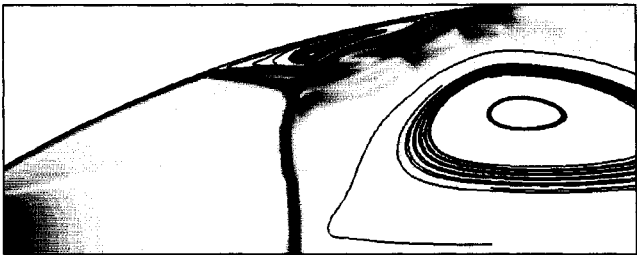


Fig. 15 Schlieren-type snapshot and instantaneous streamlines for the throttle-down process at $PR = 35$.



Fig. 16 Schlieren-type snapshot and instantaneous streamlines for the case of $PR = 30$.

thrust available from an optimum expansion nozzle operating at the same pressure ratio C_{Fopt} . An optimum expansion nozzle is one that isentropically expands the gases from chamber conditions to exactly the local ambient pressure under ideal one-dimensional conditions.

The overall agreement is very encouraging despite the exact process not being fully known, the use of a modified Baldwin-Lomax turbulence model, and a relatively coarse grid outside of the nozzle. The hysteresis phenomenon was observed, and two stable branch solutions existed. As the two branch solutions approach

the low-end turning point, the C_T difference becomes quite large, whereas the C_T difference is small near the upper-end turning point. In this bifurcation diagram, the bottom curve starting with the low-end turning point represents the branch flows with trapped reversed flow behind the Mach disk (flow can be fully separated or reattached). The top curve ending with the upper-end turning point represents the fully separated flows without trapped reversed flow behind the Mach disk. When the process of pressure change is smooth and final state pressure is bounded with its associated turning point, each branch solution could remain in the same branch

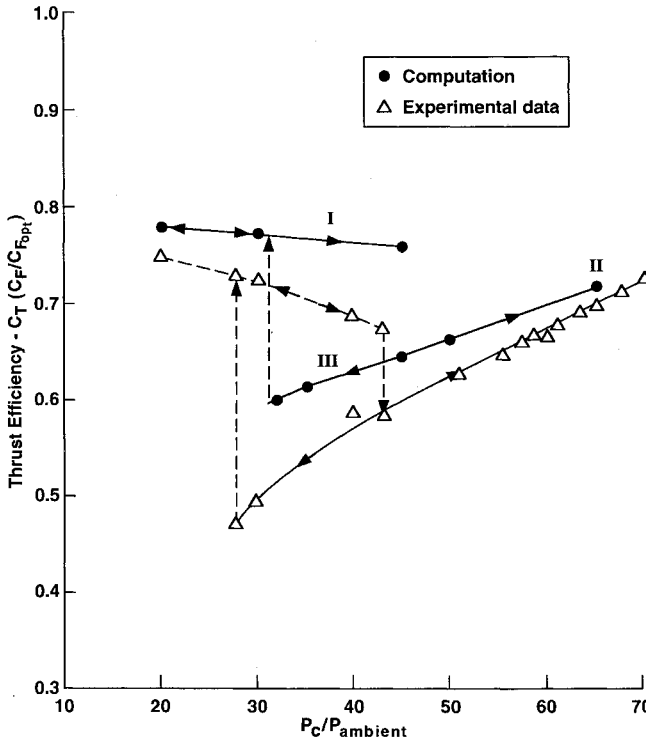


Fig. 17 Thrust efficiency vs chamber pressure.

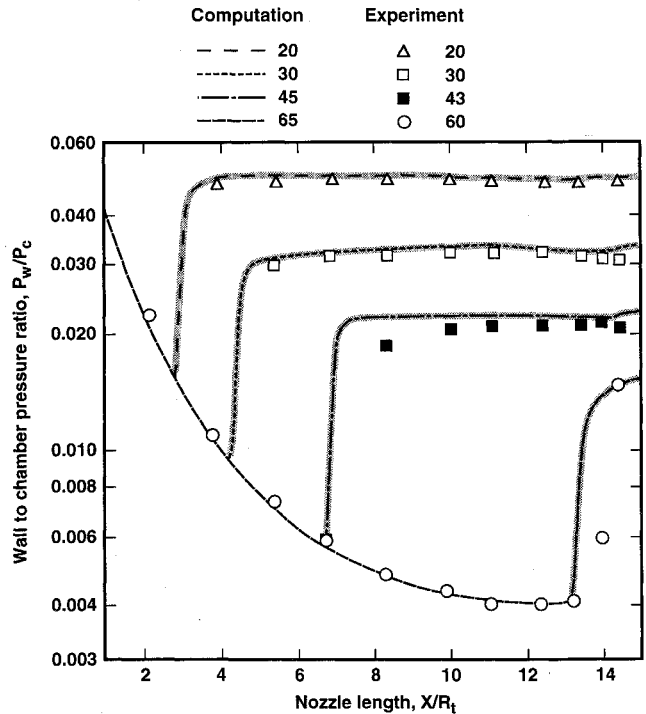


Fig. 18 Comparison of computed and experimental wall pressure for the fully separated flows.

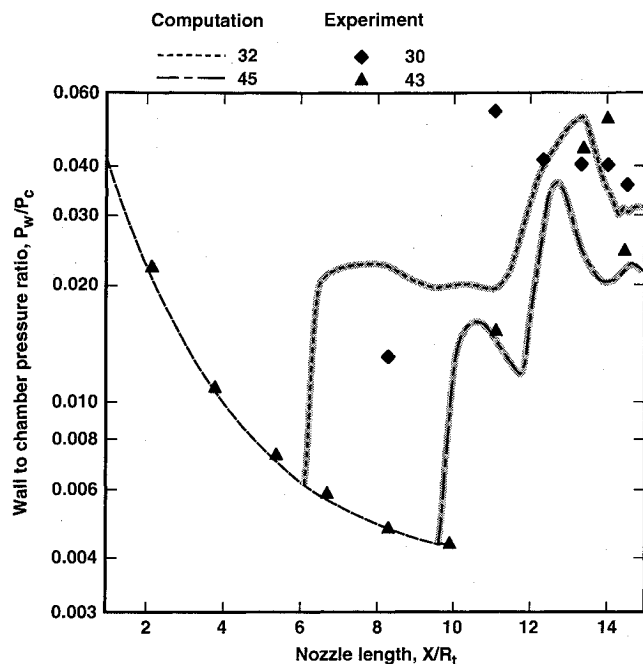


Fig. 19 Comparison of computed and experimental wall pressure for the reattached flows with a trapped vortex behind the Mach disk.

regardless of throttling or startup process. The location of the low-end turning point of hysteresis is at about $PR = 30$ in the computation and at about $PR = 27$ in the experiment. The upper-end turning point is not well resolved in the computation because of the smaller C_T jump (relative to low-end turning point) and the possible lack of grid resolution to preserve the vortical structure. The behavior of the upper-end turning point will be carefully investigated in the future.

The overall computed wall pressure data are compared with experimental data in Figs. 18 and 19. Types I and II fully separated nozzle flows are shown in Fig. 18, and the type III flows (reattached flows with vortex core trapped behind the Mach disk) are shown in Fig. 19. The small pressure unsteadiness is observed after the separation and is shaded in the figures. The locations of sharp rise of wall pressure (referred to here as points of separation) are well predicted for all of the cases (in particular for type I). Once the point of separation is closely predicted, the wall pressure is well predicted for the fully separated nozzle flows. The overall agreement for the reattached flow is also encouraging. It is interesting to note the appearance of peak pressure in Fig. 19. No pressure peak appears in the fully separated flow (Fig. 18). The high-pressure peak is associated with the flow reattachment. Both experimental and computational results confirm this. However, more pressure measurements may be needed for detailed comparison after the separation shock for the reattached flows.

IV. Conclusions

The startup and throttle-down nozzle flows for the 1/16-scale model of the J-2S rocket engine were investigated numerically for overexpanded flow conditions. During the transient startup process, the complex flow structure was revealed with various numerical probes. The resulting flowfield is substantially different from that of a one-dimensional or inviscid analysis.

The computed results as well as experimental cold-flow data indicate the hysteresis phenomenon occurring for the scale J-2S model. In the present study, three types of flow structures were seen. The first type is a fully separated flow without a vortex behind the Mach disk. The second type is a fully separated flow (but the separated region is very small) with a vortex behind the Mach disk. The third type is a separated flow reattached to the nozzle wall with a vortex behind the Mach disk.

The computed nozzle wall pressures agree with the experimental measurements for the first two types of flow. The locations of first pressure rise at the nozzle wall, after throat, are well predicted for three types of flow. High-pressure peaks were observed for the third type of flow. The trapped vortex behind the Mach disk deserves further attention.

Acknowledgments

The first two authors of this work were sponsored by Rockwell Independent Research & Development and all of the computations were performed on the NAS system. The authors thank Dale Ota and Sampath Palaniswamy for discussions, Kim Peppi for preparation of figures, and James Fenwick of Rocketdyne for providing dusty but very useful experimental documents.

References

- Shapiro, A. H., *The Dynamics and Thermodynamics of Compressible Fluid Flow*, Vol. 1, Ronald Press, New York, 1953, pp. 140, 141.
- Crocco, L., "One-Dimensional Treatment of Study Gas Dynamics," *Fundamentals of Gas Dynamics, High Speed Aerodynamics and Jet Propulsion*, Vol. 3, edited by H. W. Emmons, Princeton Univ. Press, Princeton, NJ, 1958, pp. 166, 167.
- Larson, E. W., Ratekin, G. H., and O'Connor, G. M., "Structural Response of the SSME Fuel Feedline to Unsteady Shock Oscillation," 52nd Shock and Vibration Symposium, New Orleans, LA, Oct. 1981; also *The Shock and Vibration Bulletin*, No. 52, Part 2, 1981, pp. 177–182.
- Nave, L. H., and Coffey, G. A., "Sea Level Side Loads in High-Area-Ratio Rocket Engines," AIAA Paper 73-1284, Nov. 1973.
- Chakravarthy, S. R., and Osher, S., "Computing With High-Resolution Upwind Schemes for Hyperbolic Equations," *Lectures in Applied Mathematics*, Vol. 22, Proceedings of the 1983 AMS-SIAM Summer Seminar on Large-Scale Computations in Fluid Mechanics, American Mathematical Society, 1985, pp. 57–86.
- Ramakrishnan, S., and Goldberg, U. C., "Numerical Simulation of Swept Shock/ Boundary-Layer Interactions," AIAA Paper 90-5234, Oct. 1990.
- Metwally, O., Settles, G., and Horstman, C., "An Experimental Study of the Shock Wave/Vortex Interaction Flowfield," AIAA Paper 91-1768, June 1991.
- Nave, L. H., "Evaluation of the Nozzle Incipient Separation Chamber Pressure for the SSME 470K Engine," Rockwell Internal Rept., Rocketdyne, CA, Dec. 1972.